

**The following resources related to this article are available online at  
[www.sciencemag.org](http://www.sciencemag.org) (this information is current as of November 26, 2009 ):**

**Updated information and services**, including high-resolution figures, can be found in the online version of this article at:

<http://www.sciencemag.org/cgi/content/full/312/5772/413>

**Supporting Online Material** can be found at:

<http://www.sciencemag.org/cgi/content/full/312/5772/413/DC1>

This article **cites 28 articles**, 6 of which can be accessed for free:

<http://www.sciencemag.org/cgi/content/full/312/5772/413#otherarticles>

This article has been **cited by** 56 article(s) on the ISI Web of Science.

This article has been **cited by** 2 articles hosted by HighWire Press; see:

<http://www.sciencemag.org/cgi/content/full/312/5772/413#otherarticles>

This article appears in the following **subject collections**:

Physics, Applied

[http://www.sciencemag.org/cgi/collection/app\\_physics](http://www.sciencemag.org/cgi/collection/app_physics)

Information about obtaining **reprints** of this article or about obtaining **permission to reproduce this article** in whole or in part can be found at:

<http://www.sciencemag.org/about/permissions.dtl>

example, focusing ion beams provides a different perspective, which may lead to further developments in areas such as hadron therapy for cancer treatment, accelerator physics, and inertial fusion physics. In addition to applications that use laser-driven ion beams, such a device might find application in conventional accelerator beams as a focusing or fast-switching tool.

#### References and Notes

- M. D. Perry, G. Mourou, *Science* **264**, 917 (1994).
- E. Clark *et al.*, *Phys. Rev. Lett.* **84**, 670 (2000).
- R. Snavely *et al.*, *Phys. Rev. Lett.* **85**, 2945 (2000).
- A. Maksimchuk, S. Gu, K. Flippo, D. Umstadter, V. Yu. Bychenkov, *Phys. Rev. Lett.* **84**, 4108 (2000).
- V. Malka, J. Faure, Y. Glinec, A. F. Lifschitz, *Plasma Phys. Control. Fusion* **47**, B481 (2005).
- M. Tabak *et al.*, *Phys. Plasmas* **1**, 1626 (1994).
- A. Rousse *et al.*, *Phys. Rev. Lett.* **93**, 135005 (2004).
- K. W. D. Ledingham, P. McKenna, R. P. Shinghal, *Science* **300**, 1107 (2003).
- B. A. Remington, D. Arnet, R. P. Drake, H. Takabe, *Science* **284**, 1488 (1999).
- M. Borghesi *et al.*, *Phys. Rev. Lett.* **92**, 055003 (2004).
- T. Cowan *et al.*, *Phys. Rev. Lett.* **92**, 204801 (2004).
- P. Patel *et al.*, *Phys. Rev. Lett.* **91**, 125004 (2003).
- M. Borghesi *et al.*, *Phys. Plasmas* **9**, 2214 (2002).
- S. V. Bulanov, T. Zh. Esirkepov, V. S. Khoroshkov, A. V. Kuznetsov, F. Pegoraro, *Phys. Lett. A* **299**, 240 (2002).
- I. Spencer *et al.*, *Nucl. Inst. Meth. Phys. Res. B* **183**, 449 (2001).
- M. Roth *et al.*, *Phys. Rev. Lett.* **86**, 436 (2001).
- M. Szilagy, *Electron and Ion Optics* (Plenum Press, New York, 1988).
- W. Luo, E. Fourkal, J. Li, Ch. Ma, *Med. Phys.* **32**, 794 (2005).
- B. M. Hegelich *et al.*, *Nature* **439**, 441 (2006).
- H. Schwöerer *et al.*, *Nature* **439**, 445 (2006).
- B. Wattellier *et al.*, *Opt. Lett.* **29**, 2494 (2004).
- S. J. Gitomer *et al.*, *Phys. Fluids* **29**, 2679 (1986).
- M. Allen *et al.*, *Phys. Rev. Lett.* **93**, 265004 (2004).
- J. Fuchs *et al.*, *Phys. Rev. Lett.* **94**, 045004 (2005).
- GAFCHROMIC radiochromic dosimetry films ([www.ispcorp.com/products/dosimetry/index.html](http://www.ispcorp.com/products/dosimetry/index.html)).
- L. Romagnani *et al.*, *Phys. Rev. Lett.* **95**, 195001 (2005).
- E. Lefebvre *et al.*, *Nucl. Fusion* **43**, 629 (2003).
- S. C. Wilks *et al.*, *Phys. Plasmas* **8**, 542 (2001).
- M. Key *et al.*, *Phys. Plasmas* **5**, 1666 (1998).
- These fields have been studied in detail, in planar geometry, in a previous experiment (26) and figure 3 of reference (26) shows their spatial and temporal evolution.
- S. Gordienko, A. Pukhov, personal communication.
- We thank L. Gremillet, T. Grismayer, S. Gordienko, E. Lefebvre, P. Mora, A. Pukhov, and V. Malka for fruitful discussions; E. Lefebvre for allowing us to use his PIC code CALDER; and the Commissariat à l'Énergie Atomique/Direction des Applications Militaires (CEA/DAM) for the simulations we performed on Le Centre de Calcul Recherche et Technologie (CCRT) computers. We acknowledge the support from the technical teams at LULI. This work was supported by European Union grant no. HPRIC 1999-0052, grant no. E1127 from Région Ile-de-France, and DFG TR18 and GK1203, and partly by the Queen's University of Belfast-International Research Centre for Experimental Physics (QUB-IRCEP) Distinguished Fellowship Visiting scheme and Deutscher Akademischer Austausch Dienst (DAAD).

28 December 2005; accepted 9 February 2006  
Published online 16 February 2006;  
10.1126/science.1124412  
Include this information when citing this paper.

# Bolometric Infrared Photoresponse of Suspended Single-Walled Carbon Nanotube Films

Mikhail E. Itkis, Ferenc Borondics,\* Aiping Yu, Robert C. Haddon†

The photoresponse in the electrical conductivity of a single-walled carbon nanotube (SWNT) film is dramatically enhanced when the nanotube film is suspended in vacuum. We show here that the change in conductivity is bolometric (caused by heating of the SWNT network). Electron-phonon interactions lead to ultrafast relaxation of the photoexcited carriers, and the energy of the incident infrared (IR) radiation is efficiently transferred to the crystal lattice. It is not the presence of photoexcited holes and electrons, but a rise in temperature, that results in a change in resistance; thus, photoconductivity experiments cannot be used to support the band picture over the exciton model of excited states in carbon nanotubes. The photoresponse of suspended SWNT films is sufficiently high that they may function as the sensitive element of an IR bolometric detector.

The optical properties of SWNTs, including photoconductivity, suggest outstanding potential for applications in nanoscale-sized optoelectronics (1–4). Prominent absorption features in the optical spectra of SWNTs have been widely ascribed to interband transitions associated with the series of van Hove singularities in the one-dimensional (1D) electronic density of states (5–7). However, more-recent studies suggest that the electron-hole pairs are strongly coupled in the SWNT 1D crystal lattice and that major photoexcitations are excitons, rather than free carriers (8–11). Experiments on the relaxation of photoexcitations in SWNTs (11) and two-photon excitation spec-

troscopy (12) support the exciton model and provide a large value for the exciton binding energy (0.4 eV) (12).

In the interband transition (band) model, free electrons and holes are produced upon photoexcitation, and, providing the lifetime of these carriers is sufficiently long, the spectral features in absorption and photoconductivity match the optical transitions associated with the van Hove singularities (Fig. 1A). In the exciton model, the photoexcitations occur at energies lower than the direct bandgap and give rise to neutral species that cannot directly contribute to the photoconductivity (Fig. 1A). In this situation, the excitons would have to be dissociated thermally (13) or by a large electric field (12) to produce free electrons and holes that could contribute to the photoconductivity. Exciton-related low-energy spectral features in the photoresponse would be substantially suppressed, especially at low temperatures, compared with the features corresponding to the interband transitions, and differences should arise in the absorption and photoconductivity spectra.

There are a number of reports on the photoconductivity of SWNT films deposited on optical substrates (13–15). In all cases, a very weak photoresponse with low signal-to-noise (S/N) ratio was observed despite the use of high laser powers. Nevertheless, the photoconductivity showed spectral features that coincided with the optical absorption spectrum in support of the original band model, with free carriers as the major photoexcitations (13–15). Recent photoconductivity experiments on individual SWNTs (laser power intensity of 1 kW/cm<sup>2</sup>) in a field-effect-transistor configuration gave a weak sideband in addition to the primary resonance, and the result was interpreted in a favor of the exciton model (16).

We report here on the photoconductivity of suspended SWNT films, and we are able to rationalize contradictory reports to date, as well as shed light on the nature of the optical excitations in SWNTs and the origin of the photoresponse. The extremely large photoresponse that is observed for suspended SWNT films also makes them attractive candidates for the sensitive element of an infrared (IR) bolometer.

Photoconductivity experiments were carried out with semitransparent SWNT films prepared by two different techniques. A network of as-prepared (AP) SWNTs can form in the electric arc discharge process. The network growth was initiated by the placement of stainless steel wire grids of cell size 2.54 × 2.54 cm near the plasma zone inside the electric arc chamber. The growing SWNTs drift from the plasma core toward the water-cooled walls of the arc reactor, and the wire grid nucleates the growth of an extended SWNT network that forms a continuous semitransparent SWNT film after 1 to 5 min of operation of the electric arc (fig. S1). This process leads to a high-purity film, because the SWNTs are trapped in the growing network with high probability; but typical impurities, such as nanoparticles and amorphous carbon, penetrate the thin network without becoming entangled. We

Center for Nanoscale Science and Engineering, Departments of Chemistry and Chemical and Environmental Engineering, University of California, Riverside, CA 92521-0403, USA.

\*Present address: Magyar Tudományos Akadémia, Szilárdtestfizikai és Optikai Kutatóintézete, Budapest, H 1525, Hungary.

†To whom correspondence should be addressed. E-mail: haddon@ucr.edu

have used this type of film as a reference standard for SWNT purity evaluation based on near-IR spectroscopy (17). In the second case, purified (P) SWNTs were used, and a free standing P-SWNT film was obtained by vacuum filtration of a SWNT dispersion (3, 7).

The SWNT film was suspended between two supporting blocks that also function as the electrical contacts (Fig. 1B) by placing a 0.5-mm-wide ribbon of the SWNT film across the 3.5-mm opening of a sapphire ring attached to the cold finger of the optical cryostat (Fig. 1C). At 50 K, the dc photoresponse of the AP-SWNT film to 0.04-Hz square-wave pulses (Fig. 2A) shows a resistance drop of 0.7% under an incident power of 0.12  $\mu\text{W}$  of radiation from an IR light-emitting diode (peak emission  $\lambda_p = 940$  nm), and the photoresponse is easily detectable with  $S/N \sim 100$ . The power level used in our experiments is 5 to 10 orders of magnitude lower than in previously reported photoconductivity measurements (13–16). We did not observe any detectable change of resistance in a control experiment carried out with a SWNT film supported directly on the substrate. This latter result is in agreement with the very low level of the steady-state photoconductivity signal previously reported in experiments that used much higher incident power levels (13–16). The suspension of the SWNT film in vacuum led to an enhancement of the photoconductivity response by at least 5 orders of magnitude.

The enhancement of the photoresponse of the suspended SWNT film allowed us to conduct spectral measurements with a commercial spectrophotometer at an IR power intensity of 0.1 to 1  $\mu\text{W}$ . Figure 2B shows the photoresponse of a 40-nm-thick AP-SWNT film along with its absorption spectrum. The absorption spectrum is typical of electric arc SWNTs with average diameter 1.4 nm (6), and it shows two characteristic bands that have been associated with the first and second interband transitions in semiconducting SWNTs (Fig. 2B) (5–7). The photoconductivity spectrum is virtually identical and exhibits no shift in the observed spectral positions within an accuracy of 10 meV.

To identify the nature of the photoexcitations in SWNTs, it is necessary to confirm the mechanism of the observed change in resistance. Direct photoconductivity can contribute photoexcited carriers to the electric current, or the response can be bolometric in nature, in which case the absorbed radiation heats the sample. The dramatic enhancement of the photoresponse when the thermal contact of the SWNT film with the environment is minimized by suspension supports a bolometric origin of the photoresponse, although the interaction of the SWNTs with the substrate can modify the electronic states.

There are several features that distinguish bolometric responses from free-carrier photoconductivity: (i) The bolometric response is strongly decreased by thermal coupling between

the sensitive element and the environment. (ii) The typical time constant of the bolometric response is 1 to 100 ms. (iii) The magnitude of the bolometric response depends on the temperature derivative of the resistance  $dR/dT$  (18).

Increasing the pressure in the sample chamber of the cryostat (Fig. 3A) strongly reduced the signal at pressures above 1 mtorr. The effect of the gas in thermally coupling the SWNT film to its surroundings is consistent with the bolometric nature of the photoresponse. The frequency dependence and time trace of the photosignal and the device (Fig. 3B) show a typical bolometric response time ( $\approx 50$  ms). The temperature dependence of the resistance  $R(T)$  of the suspended 1- $\mu\text{m}$ -thick film of P-SWNTs (Fig. 3C) reveals a transition at  $T \sim 230$  K from the metallic behavior, observed at high temperatures with positive  $dR/dT$ , to semiconducting behavior, with negative  $dR/dT$  at low temperatures. The photoresponse of this film presented in the form of the resistance change ( $dR$ ) under constant incident radiation (Fig. 3D) reverses sign at the resistance minimum, from positive ( $T > 230$  K) to negative ( $T < 230$  K), which is in agreement with the behavior expected for a bolometric response. If the photocarriers were responsible for the photoconductivity, the sample resistance would be expected to decrease irrespective of the sign of  $dR/dT$ . Taken together, the data establish the bolometric origin of the photoconductivity observed in suspended SWNT films.

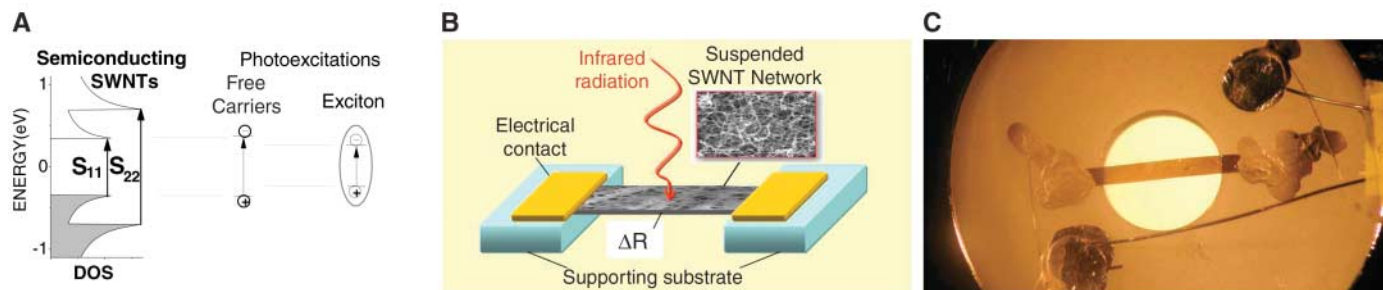
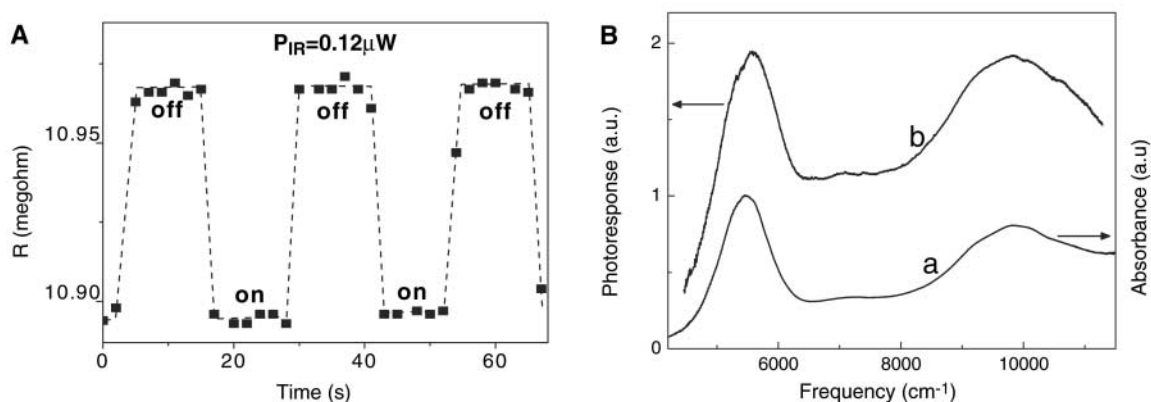


**Fig. 1.** (A) Schematic diagram of electronic density of states (DOS) and corresponding interband transitions  $S_{11}$  and  $S_{22}$  in semiconducting SWNTs (left) and schematic representation of the two types of photoexcitations: free carrier electrons and holes in the interband transition (band) model

and low-energy coupled electron-hole pairs in exciton model (right). (B) Diagram of SWNT network suspended between electrical contacts. (C) 100-nm-thick SWNT film suspended across 3.5-mm opening of a sapphire ring.

**Fig. 2.** (A) Modulation of resistance of SWNT film at 50 K under square-wave pulses of power  $P = 0.12 \mu\text{W}$  IR radiation. (B) Spectra of near-IR absorption (curve a) and electrical photoresponse (curve b) of AP-SWNT film. a.u., arbitrary units.



The direct photoconductivity component in SWNT films is likely limited by the ultrafast relaxation time of the photocarriers ( $10^{-10}$  to  $10^{-14}$  s) (11, 19). The energy of the absorbed IR radiation is efficiently transferred to the crystal lattice through strong electron-phonon interactions that increase the temperature of the film, which is observed as a photoresponse due to the temperature dependence of the resistance. In the suspended configuration, bolometric spectroscopy of long, individual SWNTs is applicable to the study of the fundamental aspects of the electronic density of states of SWNTs, which has been accomplished for single crystals of 1D compounds in charge-density-wave states (20, 21).

The absence of a spectral shift between the absorption and photoconductivity spectra (Fig. 2B) cannot be used as an argument for the band model, because the strongest bolometric response is expected at the spectral maximum of the absorbed power. Our conclusions regarding the bolometric nature of the photoresponse in SWNT films suggests that previous arguments in favor of the band model, which are based on an interpretation of direct photoconductivity (contribution of photoexcited electrons and holes to the transport properties), should be reexamined. It is possible that direct photoconductivity may be observable in individual SWNTs (16); in this configuration, the bolometric response is suppressed by the efficient dissipation of the heat, because the thermal conductivity of the SWNTs is not limited by the intertube junctions, which dominate the thermal and electrical resistance in the case of SWNT films (22, 23).

Thin films of SWNTs have already demonstrated outstanding performance in gas and biosensing applications (24–26) and as a semi-transparent conducting coating for large-area flexible optoelectronics (3, 22, 27, 28). The strong bolometric response reported here shows the potential of SWNT thin films to function as the sensitive elements of infrared bolometers; in our experiments, we found that in the absence of the cold optical filter that is used to block the blackbody radiation from the environment, the temperature of the SWNT sample rose more than 100 K above the temperature of the supporting sapphire ring at 10 K. The strong thermal response of SWNTs to incident radiation may be responsible for the ignition of SWNTs that has been observed when the material is exposed to a conventional photographic flashlight (29). The absorption coefficient of SWNTs is extremely high ( $10^4$  to  $10^5$   $\text{cm}^{-1}$ ) (fig. S2), at least 1 order of magnitude greater than that of mercury-cadmium-telluride, the most popular photoconductor for 2D arrays of IR photodetectors (18). Furthermore, the strong absorption of SWNT thin films extends from the ultraviolet to the far-IR region, (6) and a 100-nm-thick film absorbs >70% of the incident radiation. At this thickness, the SWNT film has an extremely low mass (ng), thus satisfying the low-heat capacity requirement of the bolometer sensitive element (18).

A high negative value of the temperature coefficient of resistance (TCR) of the bolometer sensitive element is required to efficiently transfer temperature modulation into an electrical signal (18). The temperature dependence of resistance

$R(T)$  of three thin SWNT films used in laboratory prototype SWNT IR bolometers is given in Fig. 4A, and Fig. 4B shows the corresponding voltage responsivities (ratio of output voltage to incident power). The resistance of the film of P-SWNTs of 1- $\mu\text{m}$  thickness shows a very weak temperature dependence with a change in the sign of the slope from metallic to semiconducting around 230 K (Fig. 3C), and this film shows a low responsivity especially at high temperatures (Fig. 4B, curve a). By decreasing the thickness of the film to 100 nm and annealing the film in vacuum at 670 K, it was possible to eliminate the metallic behavior, increase the TCR, and substantially enhance the responsivity over the entire temperature range. The strongest change of resistance with temperature [ $R(4.2\text{ K})/R(300\text{ K}) = 100$ ], and highest responsivity (up to 1000 V/W), was obtained for a 40-nm-thick film of AP-SWNTs. We registered a noise power density of less than  $10^{-14}$   $\text{V}^2/\text{Hz}$  in the frequency range 1 to 100 Hz, which is comparable to the lowest noise levels reported for carbon nanotube films (27, 30).

The AP-SWNT film shows a TCR between 1 and 2.5% in the 330 to 100 K temperature range (fig. S3); these values are comparable with the TCR of vanadium dioxide, the most common thermistor material used in the fabrication of micromachined silicon bolometers (18). The TCR can be further increased by reducing the film thickness, modifying the processing conditions, and by chemical functionalization of the SWNTs (23). The SWNT film can be envisioned as a network of individual SWNTs or small bundles in which electrical resistance and its temperature dependence are dominated by tunneling at the intertube junctions (22, 23). Modification

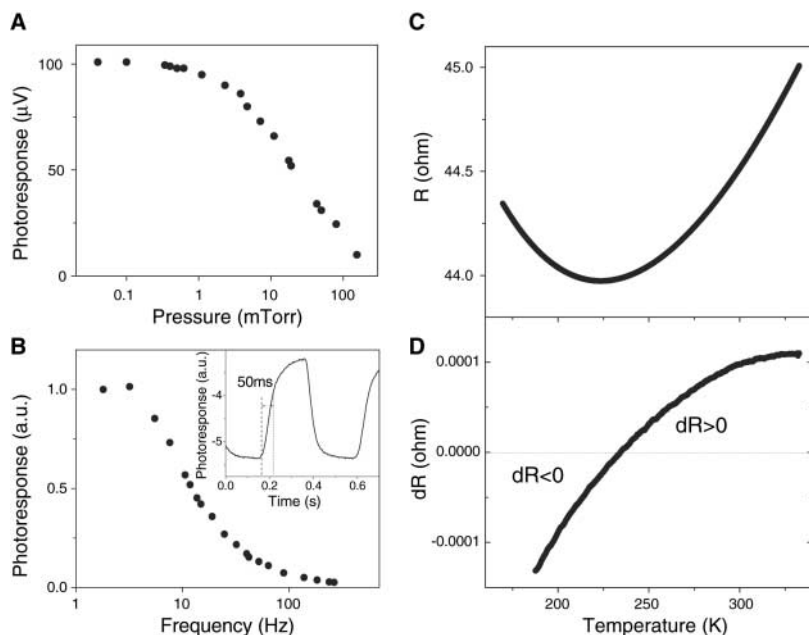


**Fig. 3.** Demonstration of bolometric nature of photoresponse. (A) Dependence of photoresponse on pressure in the cryostat. (B) Dependence of photoresponse on chopping frequency. (Inset) Time trace of square-wave modulated photoresponse with characteristic rise time of 50 ms. (C) Temperature dependence of resistance of 1- $\mu\text{m}$ -thick film of purified SWNTs with minimum at 230 K caused by transition from metallic to semiconducting behavior. (D) Reverse of the sign of photoresponse caused  $dR$  at the resistance minimum.

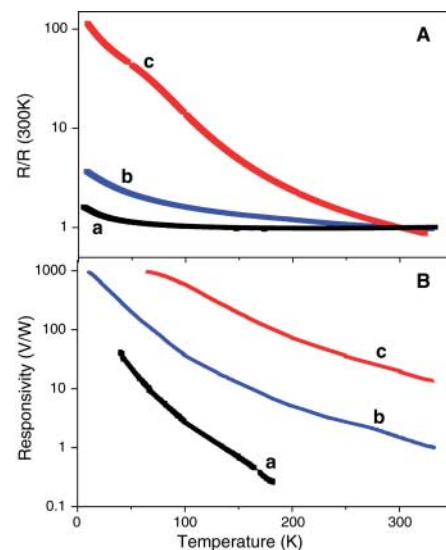


**Fig. 4.** (A) Temperature dependences of resistance of three SWNT films: (i) 1- $\mu\text{m}$ -thick film of purified SWNTs (curve a); (ii) 100-nm-thick film of purified SWNTs annealed in vacuum at 670 K (curve b); and (iii) 40-nm-thick AP-SWNTs film (curve c). (B) Corresponding voltage responsivity of infrared bolometers made from these films.

of these junctions by chemical functionalization (23) or physical processing can markedly increase the TCR as shown in the annealing experiment (fig. S3). The presence of intertube junctions dramatically decreases the efficiency of heat transport along the SWNT film, thereby thermally insulating the sensitive element from the supporting substrate, which enhances the temperature response (18). Optimization of the room-temperature performance of the SWNT-based bolometer may provide a cost-efficient alternative to pyroelectric detectors, vanadium dioxide, and amorphous silicon-based bolometer arrays (18).

The SWNT networks used here are a mixture of semiconducting and metallic SWNTs; metallic pathways present within such networks reduce the temperature dependence of the resistance (23). The ultimate enhancement of the TCR would be achieved by the exclusive use of semiconducting SWNTs, but even with current preparations, the implementation outlined above in conjunction with recent advances in carbon nanotube thin film preparation technology (3, 7, 22, 27, 28) allows the manufacture of high-density 2D arrays of SWNT bolometers that are suitable for applications in thermal imaging, spectroscopy, and infrared astronomy (18).

## References and Notes

1. J. A. Misewich *et al.*, *Science* **300**, 783 (2003).
2. M. Freitag *et al.*, *Phys. Rev. Lett.* **93**, 076803 (2004).
3. Z. Wu *et al.*, *Science* **305**, 1273 (2004).
4. P. W. Barone, S. Baik, D. A. Heller, M. S. Strano, *Nat. Mater.* **4**, 86 (2005).
5. M. S. Dresselhaus, G. Dresselhaus, P. Avouris, Eds., *Carbon Nanotubes: Synthesis, Structure, Properties and Applications*, vol. 80 (Springer-Verlag, Berlin, 2001).
6. M. E. Itkis *et al.*, *Nano Lett.* **2**, 155 (2002).
7. F. Hennrich *et al.*, *Phys. Chem. Chem. Phys.* **4**, 2273 (2002).
8. T. Ando, *J. Phys. Soc. Jpn.* **66**, 1066 (1997).
9. C. D. Spataru, S. Ismail-Beigi, L. X. Benedict, S. G. Louie, *Phys. Rev. Lett.* **92**, 077402 (2004).
10. V. Perebeinos, J. Tersoff, P. Avouris, *Phys. Rev. Lett.* **92**, 257402 (2004).
11. C.-X. Sheng, Z. V. Vardeny, A. B. Dalton, R. H. Baughman, *Phys. Rev. B* **71**, 125427 (2005).
12. F. Wang, G. Dukovic, L. E. Brus, T. Heinz, *Science* **308**, 838 (2005).
13. Y. Matsuoka *et al.*, *Sci. Technol. Adv. Mater.* **4**, 47 (2003).
14. A. Fujiwara *et al.*, *Carbon* **42**, 919 (2004).
15. A. Mohite, S. Chacabarty, P. Gopinath, G. U. Sumanasekera, B. W. Alphenaar, *App. Phys. Lett.* **86**, 061114 (2005).
16. X. Qiu, M. Freitag, V. Perebeinos, P. Avouris, *Nano Lett.* **5**, 749 (2005).
17. M. E. Itkis *et al.*, *Nano Lett.* **3**, 309 (2003).
18. M. Henini, M. Razeghi, *Handbook of Infrared Detection Technologies* (Elsevier Advanced Technology, Kidlington, Oxford, UK, 2002).
19. F. Wang, G. Dukovic, L. E. Brus, T. Heinz, *Phys. Rev. Lett.* **92**, 177401 (2004).
20. S. L. Herr, G. Minton, J. W. Brill, *Phys. Rev. B* **33**, 8851 (1986).
21. M. E. Itkis, F. Y. Nad', *JETP Lett.* **39**, 448 (1984).
22. E. Artukovic, M. Kaempgen, D. S. Hetch, S. Roth, G. Gruner, *Nano Lett.* **5**, 757 (2005).
23. E. Bekyarova *et al.*, *J. Am. Chem. Soc.* **127**, 5990 (2005).
24. E. Bekyarova *et al.*, *J. Phys. Chem. B* **108**, 19717 (2004).
25. E. S. Snow, F. K. Perkins, E. J. Houser, S. C. Badescu, T. L. Reinecke, *Science* **307**, 1942 (2005).
26. A. Star, T.-R. Han, V. Joshi, J.-C. P. Gabriel, G. Gruner, *Adv. Mater.* **16**, 2049 (2004).
27. M. Zhang *et al.*, *Science* **309**, 1215 (2005).
28. M. Kaempgen, G. S. Duesberg, S. Roth, *Appl. Surf. Sci.* **252**, 425 (2005).
29. P. M. Ajayan *et al.*, *Science* **296**, 705 (2002).
30. P. G. Collins, M. S. Fuhrer, A. Zettl, *Appl. Phys. Lett.* **76**, 894 (2000).
31. Supported by the U.S. Department of Defense/Defense Advanced Research Projects Agency/Defense Microelectronics Activity grants DMEA90-02-2-0216, H94003-04-2-0404, and H94003-05-2-0504. F.B. was supported by a Fulbright Association and Hungarian Scientific Research Fund (OTKA) T049338.

## Supporting Online Material

www.sciencemag.org/cgi/content/full/312/5772/413/DC1  
Materials and Methods  
Figs. S1 to S3

1 February 2006; accepted 21 March 2006  
10.1126/science.1125695

# Atomic Pillar–Based Nanoprecipitates Strengthen AlMgSi Alloys

J. H. Chen,\* E. Costan, M. A. van Huis, Q. Xu, H. W. Zandbergen

Atomic-resolution electron microscopy reveals that pillarlike silicon double columns exist in the hardening nanoprecipitates of AlMgSi alloys, which vary in structure and composition. Upon annealing, the Si<sub>2</sub> pillars provide the skeleton for the nanoparticles to evolve in composition, structure, and morphology. We show that they begin as tiny nuclei with a composition close to Mg<sub>2</sub>Si<sub>2</sub>Al<sub>7</sub> and a minimal mismatch with the aluminum matrix. They subsequently undergo a one-dimensional growth in association with compositional change, becoming elongated particles. During the evolution toward the final Mg<sub>5</sub>Si<sub>6</sub> particles, the compositional change is accompanied by a characteristic structural change. Our study explains the nanoscopic reasons that the alloys make excellent automotive materials.

Aluminum is essential to modern civilizations because of its light weight, strength, and workability. Its many applications include fuel-efficient transportation vehicles (e.g., it comprises about 80% of a commercial aircraft's unloaded weight), building construction, and food packaging. Pure aluminum is soft and has little strength or resistance to plastic deformation. However, alloyed with small amounts of other elements, it can provide the strength of steel at only half the weight. With thermal treatments, the added alloying elements can form nanometer-sized precipitates, which act

as obstacles to dislocation movement in the crystal (atomic matrix), strengthening the aluminum. This phenomenon is known as precipitation hardening, and the hardening nanoprecipitates are named GP zones after the pioneer work by Guinier and Preston on AlCu alloys (1, 2).

AlMgSi accounts for a large percentage of the total aluminum production in the world. With appropriate pre-aging treatments, AlMgSi alloys can be pressed easily into a given form and then strengthened rapidly by annealing for a very short duration (<30 min) at about 180°C [i.e., by a characteristic two-step age-hardening process (3)]. This important property of AlMgSi alloys, called the quick-bake hardening response, has led to increased applications in the automotive industry (3–7), such as outer panel materials that have a strength/weight ratio optimal for fuel efficiency and environmental

protection. It has long been understood that AlMgSi alloys are strengthened when needle-like monoclinic precipitates form (5–14), but to date little is known about the structures of the particles responsible for the quick-bake hardening response (5–7). Whereas the final structure of the needlelike particles has been determined (8, 9), their early-stage development is difficult to characterize.

Because the nanoprecipitate structures are not well understood, the hardening nanoparticles in AlMgSi alloys are named ambiguously: They are referred to as GP(I) and GP(II) zones, pre-β' and β' phases, or Si/Mg co-clusters and GP zones in the early stages (4–11). The essential questions remain: How many different hardening particles exist, and how do they transform from one to another? To answer these questions, we used high-resolution transmission electron microscopy (HRTEM) and computational analysis to assess their initial structures.

We studied aluminum that was alloyed with 0.43% Mg and 1.2% Si (15). The homogenized alloy was heated at 560°C and then water quenched to 20°C. The best quick-bake hardening response can be achieved if the hardening annealing is performed immediately after water quenching. However, this is not practical for automotive body sheet applications, because the sheets have to be stored (up to months) and shipped at room temperature. Any storage (natural aging) will quickly degrade the alloy's quick-bake hardening response because of the formation of natural-aging clusters, which delay the formation of the hardening particles upon annealing (4–7). Hence, for advanced applications, pre-aging has

Netherlands Institute for Metals Research and Kavli Institute of Nanoscience, Delft University of Technology, Lorentzweg 1, 2628 CJ Delft, Netherlands.

\*To whom correspondence should be addressed. E-mail: j.h.chen@tnw.tudelft.nl